Sciencexpress Reports

# Taxel-Addressable Matrix of Vertical-Nanowire Piezotronic Transistors for Active/Adaptive Tactile Imaging

**Wenzhuo Wu,[1]* Xiaonan Wen,[1]* Zhong Lin Wang[1,2]†**

[1]School of Materials Science and Engineering, Georgia Institute of Technology, Atlanta, GA 30332, USA.
[2]Beijing Institute of Nanoenergy and Nanosystems, Chinese Academy of Sciences, Beijing, China.

*These authors contributed equally to this work.

†Corresponding author. E-mail: zhong.wang@mse.gatech.edu

**Designing, fabricating and integrating arrays of nanodevices into a functional system is the key for transferring nano-scale science into applicable nanotechnology. We report large-array three-dimensional (3D) circuitry integration of piezotronic transistors based on vertical zinc oxide nanowires as active taxel-addressable pressure/force-sensor matrix for tactile imaging. Using the piezoelectric polarization charges created at metal-semiconductor interface under strain to gate/modulate transport process of local charge carriers, piezotronic effect has been applied to design independently addressable two-terminal transistor arrays, which convert mechanical stimuli applied on the devices into local electronic controlling signals. The device matrix has been demonstrated for achieving shape-adaptive high-resolution tactile imaging and self-powered, multi-dimensional active sensing. The 3D piezotronic transistor array may have applications in human-electronics interfacing, smart skin and micro/nano-electromechanical systems.**

Progress has been achieved in implementing flexible pressure sensor based on array of tactile pixels (taxels) for mimicking tactile sensing capabilities of human skins, in which electronic components like traditional planar field-effect-transistors (FETs) act as read-out elements for detecting pressure-induced property change in the pressure-sensitive media (*1–6*). Efforts are devoted to minimize the effect of substrate strain on performance of these electronic components while increasing the flexibility of the substrate (*1–3*, *7*). This scheme of pressure sensing not only requires complicated system integration of heterogeneous components but also lacks direct and active interfacing between electronics and mechanical actuations. Moreover, the sizes of as-fabricated taxels are of hundreds of microns to even tens of millimeters, severely limiting device density and spatial resolution. Although architectures like three-dimensional (3D) integrated circuits and wrap-gate vertical transistor present the attractive approaches to achieve high-density assembly of functional nanodevices (*8–11*), it is cumbersome to fabricate the gate electrode and manage interconnect layout for effectively controlling individual device within a high-density matrix (schematic of a representative wrap-gate nanowire (NW) FET is shown in Fig. 1A (left)).

Recently, using piezoelectric-semiconductor NWs that typically have wurtzite and zinc blend structures, such as ZnO and GaN, a fundamental design of piezotronic transistor was introduced (*12–15*), which has a two-terminal metal-semiconductor-metal (MSM) structure and its charge carrier transport is modulated by the piezoelectric-polarization-charge induced inner-crystal potential in the NW at the contacts. Piezotronic effect differs from the conventionally utilized piezoresistance effect in that the latter results from change in bandgap, charge carrier density or density of states in the conduction band of the strained semiconductor material which functions as a scalar "resistor", while piezotronic effect arises due to the polarization of non-mobile ions in the crystal. Therefore piezoresistive effect is a symmetric volume effect without polarity, while piezotronic effect is an interface effect which asymmetrically modulates local contacts at different terminals of the device due to the polarity of the piezoelectric potential (piezopotential) (*15–18*). The magnitude and polarity of piezopotential within piezotronic transistor changes according to the local stress/force, resulting in a direct control over local Schottky barrier heights (SBHs) and hence the corresponding transport characteristics of the piezotronic transistor by induced strain. Consequently, no applied electrical-gate-voltage is required for piezotronic transistor. Strain-gated piezotronic transistors operated through the modulation of local contact characteristics and charge carrier transport by strain-induced ionic polarization charges at the interface of metal-semiconductor contact (*13*, *16–20*), which is different from the voltage-gated operation of traditional FET.

The elimination of wrap gate also offers a new approach for 3D structuring. The basic structure of a 3D strain-gated vertical piezotronic transistor (SGVPT) is depicted in Fig. 1A (right), consisting of one or multiple vertically-grown ZnO NWs in contact with bottom and top electrodes. ZnO NW experiences axial strain when subjected to external mechanical deformation, with piezopotential induced inside the NW due to polarization of non-mobile ions distributed at the two ends (*15*, *17*, *18*). The local contact profile and carrier transport characteristics across the Schottky barrier, formed between ZnO NW and metal electrodes, is effectively controlled by the polarization-charge-induced potential. Electrical characteristics of the two-terminal SGVPT are therefore modulated by external mechanical actions induced strain, which essentially functions as a gate signal for controlling SGVPT.

By combining the patterned in-place growth of vertically aligned ZnO NWs with state-of-the-art microfabrication techniques, large-scale integration of SGVPT array can be obtained. Figure 1B illustrates the schematic of the SGVPT array with taxel density of 92 × 92 in 1 $cm^2$ (234 taxels per inch (TPI)). The equivalent circuit diagram of the SGVPT array is displayed in Fig. 1C to demonstrate the operation scheme of the SGVPT devices circuitry. The taxel area density of SGVPT array is 8464/$cm^2$, which is higher than the number of tactile sensors in recent reports (~ 6-27/$cm^2$) (*1–3*, *6*) and mechanoreceptors embedded in the human fingertip skins (~ 240/$cm^2$) (*21*). A detailed description of the device fabrication process is shown in the supplementary materials and figs. S1 and S2. Briefly, the active array of SGVPTs is sandwiched between the top and bottom Indium Tin Oxide (ITO) electrodes, which are aligned in orthogonal cross-bar configurations. A thin layer of Au is deposited between the top/bottom surfaces of ZnO NWs and top/bottom ITO electrodes, respectively, forming Schottky contacts with ZnO NWs. A thin layer of Parylene C (1 μm thickness) is conformably coated on the SGVPT device as the moisture/corrosion barrier. Well-aligned ZnO NWs, synthesized by a low-temperature hydrothermal method (*22*), function as the active channel material of SGVPT and help reduce the stochastic taxel-to-taxel variation to ensure uniform device performance. Figure 1D and fig. S3 show the SGVPT array after etch-

ing-back the SU 8 layer and exposing top portions (~ 20 μm) of the ZnO NWs (see supplementary materials for fabrication details). The as-synthesized ZnO NWs show single-crystallinity (fig. S3). The three-dimensional nature and vertical hierarchy of the SGVPT assembly is revealed by topological profile imaging (Fig. 1E) using an optical non-contact profilometer (Wyko Profilometer NT3300), which measures the phase change of light reflected from various heights in the structure by interferometry. The high degree in alignment and uniformity of SGVPT array in three dimensions (~ 30 μm in height and 20 μm × 20 μm in taxel size) is enabled by process control in both the bottom-up synthesis of NWs and top-down fabrication of circuitry. The use of a two-terminal configuration based on piezotronic effect simplifies the layout design and circuitry fabrication while maintains effective control over individual devices. Transparency and flexibility of SGVPT array devices are demonstrated in Fig. 1F and figs. S4 and S5.

By fixing on one top electrode, the 92 taxels between this top electrode and corresponding bottom electrodes can be addressed and characterized individually (supplementary materials). Representative data from 23 taxels in a typical single-channel line-scan (1 × 92) measurement for SGVPT array device is shown in Fig. 2. The corresponding topological profile images (top view) of the selected taxels are displayed at the top of Fig. 2A. Current response from each taxel under 1 V bias, with and without external pressure (20 kPa) applied to a localized region (around taxels 45 and 46), is recorded and plotted with color representing ratio of the response amplitude for each taxel in an 80-s window. It can be seen that for this single-channel array of SGVPTs, pressure variations can be distinguished with both high sensitivity and spatial resolution (taxel periodicity ~ 100 μm). The dominant mechanism for the transport property of SGVPT is piezotronic effect rather than piezoresistance effect, as experimentally confirmed and elaborated in details (fig. S6) (*15*, *17*, *18*). Data from single-channel conductance measurement in temporal domain are compiled and shown in Fig. 2B and fig. S7 to further illustrate the dynamic response of SGVPT devices. Distinctive changes in conductance can be observed for taxels 45 and 46 before and after applying the localized pressure. Although the measured response time (rise time) of ~ 0.15 s for SGVPT taxel (fig. S7) is larger than that of human fingertips (~ 30-50 ms), it is comparable to previously reported values of 0.1 s (*1*). These results indicate that SGVPT array can respond to both static and some dynamic stimuli. The response time can be further improved in future design by integrating local on-site signal-processing circuits with SGVPT array (*23*). The pressure sensitivity of a single SGVPT is also probed and shown in Fig. 2C (for taxel 46). From the measured variations in current responses by consecutively increasing the pressure load applied at fixed location, the SGVPT device demonstrates high sensitivity for detecting pressure change, particularly in low-pressure regions (< 10 kPa). The modulation effect of applied pressure is shown from the plot of current variations against pressure changes (top right inset of Fig. 2C). It can be seen that the maximum pressure SGVPT taxel can still distinguish without "saturation" is around 30 kPa, above which the current saturates. The observed sensing range of a few kPa to ~30 kPa for SGVPT array is well matched to the 10-40 kPa range which a human finger applies to sense texture and shape (*24*). The sensitivity for SGVPT, defined as $S = d\mathrm{G}_{\mathrm{SGVPT}}/d\mathrm{P}$, is around 2.1 $\mu\mathrm{S}\cdot\mathrm{kPa}^{-1}$, which arises from the change in carrier transport of the SGVPT by applied pressure due to corresponding modulation of barrier height at the reversed biased Schottky contact by strain-induced piezopotential (*15*, *17*, *18*). Specifically, the conductance of SGVPT device is dictated by the reversed biased Schottky contact, which is formed between ZnO NWs and top electrodes in this case. Upon applying the normal stress, accumulation of piezoelectric charges at both Schottky contacts induce the distribution of piezopotential. Due to the orientation of the polar *c* axis in the as-synthesized ZnO NWs (indicated by the red arrowhead in Fig. 1A, right), negative piezopotential is induced at the reversed biased top Schottky contact, which raises the barrier height at that contact and hence decreases the transport conductance of the SGVPT taxel, as depicted by the schematic band diagrams in Fig. 2C (bottom left inset) and fig. S6. The operation of SGVPT device is therefore based on barrier-interface-modulation that enables enhanced sensitivity and efficiency compared to the channel-modulation operation in conventional FETs. The quality of the Schottky contacts has been characterized (supplementary materials and fig. S8). The Schottky barrier heights (SBHs) and ideality factors of the formed contacts for devices without extra oxygen plasma treatment before depositing the top electrode are 0.419 ± 0.011 eV and 5.84 ± 1.29 respectively, while the SBHs and ideality factors of the formed contacts for devices with extra oxygen plasma treatment before depositing the top electrode are found to be 0.575 ± 0.013 eV and 2.17 ± 0.33 respectively, indicating that the qualities of as-fabricated Schottky contacts have been improved by the oxygen plasma treatment (*19*).

The feasibility and scalability of the proposed integration scheme is demonstrated by the successful fabrication of the 92 × 92-taxel SGVPT array, enabling a 15-to-25-fold increase in number of taxels and 300-to-1000-fold increase in taxel area density compared to recent reports (*1*–*3*, *6*). The output current of each individual SGVPT taxel is measured and averaged within a short duration window of 10 ms. By monitoring the output current of each independently-functioning SGVPT in the matrix, spatial profile of applied pressure can be readily imaged by multiplexed-addressing all of the taxels. Two-dimensional current contour plot is thus obtained by registering the measured current to the corresponding taxel coordinates along *x* (bottom electrode) and *y* (top electrode) axes. Metrology mapping has then been performed on the fully integrated SGVPT array without applying pressure (Fig. 3A, inset), demonstrating that all of the 8464 SGVPTs within the array are functional. The subsequent statistic investigation reveals the good uniformity in electrical characteristics among all of the taxels, with 95% of the SGVPTs possessing current values in the narrow range of 13.7 ± 2.73 μA under 1 V bias (Fig. 3A). The uniformity in current distribution of SGVPTs can be further improved by optimizing the fabrication process, such as achieving uniform amount of ZnO NWs within each taxel (fig. S3) and obtaining even profiles in the etch-back step of SU 8 layer. To demonstrate the tactile sensing capability of the integrated SGVPT array, a normal stress of ~ 25 kPa is applied to the device by pressing a hexagonal-shape mold. As depicted in Fig. 3B, which presents the difference between current values for each taxel before and after applying the normal stress, the profile of applied stress can be spatially imaged.

SGVPT devices are still operational and capable of imaging the spatial profile of applied pressure after 24-hour immersion in 23°C deionized (DI) water and 37°C 0.9% saline solution as well as after 6-hour immersion in 65°C DI water and 65°C 0.9% saline solution (figs. S9 and S10), indicating a good stability and feasibility of SGVPT array operation for future applications like in vivo physiological sensing in complex environments. Deteriorated adhesion between the encapsulation SU 8 layer in SGVPT array and substrate was observed for devices after prolonged immersion (12 hours) in both solutions at 65°C. It is interesting to note even in such cases, top electrodes and taxels remain in good shape while only rupture of bottom electrodes can be seen (fig. S10).

The multi-dimensional sensing capability is further demonstrated in Fig. 3C, exhibiting the potential of not only resolving the stress profile spatially but also registering the stress variations to the mapped geometrical pattern, as enabled by the uniform sensitive response of taxels across the whole array and the high spatial taxel density. For a better demonstration of this concept, SGVPT device fabricated on solid substrate like silicon is used here. Normal stresses with well-determined values as well as spatial locations are applied to the device using the 3-axis stage and force gauge (supplementary materials). The first group of six normal local stresses, each around 8.1 kPa, are applied to the array at

pre-programmed locations in the sequence indexed from 1 to 6, with the corresponding contours imaged and organized, as shown in Fig. 3C, to emulate the writing calligraphy of letter "A" (outlined by the white dashed lines). This process is achieved by varying the *x* and *y* coordinates while keeping the *z* coordinate constant in the control interface of the 3-axis stage. It can be seen from Fig. 3C that spatial profiles of all of the six applied stresses can be distinguished and mapped electronically. The second group of six normal stresses with the same locations are subsequently applied to the array in the same sequence, except that the stresses applied at sites 2 and 3 are increased to ~ 20 kPa with stresses at the rest four sites unchanged. The corresponding mapped contours are again recorded and organized, as shown in Fig. 3C. These results demonstrate the potential of utilizing SGVPT array for future applications such as multi-dimensional signature recording, which not only records the calligraphy or signature patterns, when people write, but also registers the corresponding pressure/force applied at each location/taxel (dedicated by the taxel resolution) by the person. This augmented capability can essentially provide means for realizing personal signature recognition with unique identity and enhanced security.

The real time detection of shape changes caused by stretching or twisting is a desirable feature for sensors embedded in an artificial tissue or prosthetic device. Figure 4A shows optical photographs of the experimental setup for investigating the feasibility of SGVPT array for shape-adaptive sensing. A rectangular supporting object is fixed to the platen of probe station, directly beneath the central region of SGVPT array (Fig. 4A). After the probe pins are in contact with the pads at the peripheral of SGVPT devices, the platen is further raised up so that SGVPT device is hunched by the underneath supporting object (Fig. 4A, bottom) with the radius of curvature ~ 79.63 mm. The measured difference in taxel currents with and without the underneath supporting object is mapped and plotted in Fig. 4B, illustrating a good agreement between the detected shape change of SGVPT array (dark blue regions) and the physical shape of the supporting object beneath the SGVPT device (outlined by white dashed lines). The shape-adaptive sensing capability is further examined by applying an additional localized stress to the bent SGVPT array, using the same setup in Fig. 3, B and C, as depicted by the 3D schematic drawing in Fig. 4B (bottom right). The measured variations in taxel current values between bent SGVPT array with extra stress and unstrained SGVPT array is imaged and plotted in Fig. 4B. A clearer demonstration of the data can be obtained by numerical subtraction (Fig. 4B, "B2-B1"), which gives rise to spatial imaging of the additionally applied stress when the shape of the SGVPT device changes. Such shape-adaptive sensing has also been investigated for other radii of curvatures (fig. S11). Because of the relatively large thickness of the SGVPT device (mainly contributed by the PET substrate which is 500 μm thick), the saturation of SGVPT response under large pressure (as shown in Fig. 2C) and the constraints of measurement setup (probes on probe card have limited movement in vertical direction), the SGVPT array is unable to sense the change in device shape and further distinguish the applied pressure when radii of curvature is smaller than 30-35 mm (Fig. 4C). The detectable range of shape deformation as well as corresponding shape-adaptive sensing can be improved by engineering the device into more compliant form to reduce the strain induced in SGVPT due to change in device shape (fig. S12).

Cyclic bending has been further performed on SGVPT array for investigating the reliability and stability of device operations. In order to accelerate the aging process, SGVPT array has been repeatedly bent to a very small radius of curvature (15 mm as shown in fig. S13) at 2-Hz frequency. Metrology mapping has then been performed on SGVPT array and plotted for comparison with that of device before the cyclic bending. No significant degradation can be observed in operation of SGVPT array even after 1000-cycle bending, suggesting good stability in device operation.

Using two-terminal piezotronic transistors, we fabricated large-scale array of strain-gated vertical piezotronic transistors using patterned and vertically-aligned NWs. By replacing the externally applied voltage with the inner-crystal piezopotential and eliminating the gate electrode as for a conventional FET, it is possible to fabricate high-density array of SGVPTs with high-resolution imaging capability. The SGVPT devices can function as active and self-powered tactile sensors by directly converting applied mechanical actuations into electrical control signals without applying gate voltage (fig. S14) and act as a fundamental component for piezotronics (*15*, *25*).

**References and Notes**


1. K. Takei *et al*., Nanowire active-matrix circuitry for low-voltage macroscale artificial skin. *Nat. Mater.* **9**, 821 (2010). doi:10.1038/nmat2835 Medline
2. S. C. B. Mannsfeld *et al*., Highly sensitive flexible pressure sensors with microstructured rubber dielectric layers. *Nat. Mater.* **9**, 859 (2010). doi:10.1038/nmat2834 Medline
3. T. Someya *et al*., A large-area, flexible pressure sensor matrix with organic field-effect transistors for artificial skin applications. *Proc. Natl. Acad. Sci. U.S.A.* **101**, 9966 (2004). doi:10.1073/pnas.0401918101 Medline
4. D. J. Lipomi *et al*., Skin-like pressure and strain sensors based on transparent elastic films of carbon nanotubes. *Nat. Nanotechnol.* **6**, 788 (2011). doi:10.1038/nnano.2011.184 Medline
5. D. H. Kim *et al*., Epidermal electronics. *Science* **333**, 838 (2011). doi:10.1126/science.1206157 Medline
6. T. Sekitani *et al*., Organic nonvolatile memory transistors for flexible sensor arrays. *Science* **326**, 1516 (2009). doi:10.1126/science.1179963 Medline
7. D. H. Kim *et al*., Stretchable and foldable silicon integrated circuits. *Science* **320**, 507 (2008). doi:10.1126/science.1154367 Medline
8. A. Javey, S. Nam, R. S. Friedman, H. Yan, C. M. Lieber, Layer-by-layer assembly of nanowires for three-dimensional, multifunctional electronics. *Nano Lett.* **7**, 773 (2007). doi:10.1021/nl063056l Medline
9. J. H. Ahn *et al*., Heterogeneous three-dimensional electronics by use of printed semiconductor nanomaterials. *Science* **314**, 1754 (2006). doi:10.1126/science.1132394 Medline
10. S. Nam, X. C. Jiang, Q. H. Xiong, D. Ham, C. M. Lieber, Vertically integrated, three-dimensional nanowire complementary metal-oxide-semiconductor circuits. *Proc. Natl. Acad. Sci. U.S.A.* **106**, 21035 (2009). doi:10.1073/pnas.0911713106 Medline
11. T. Bryllert, L. E. Wernersson, L. E. Froberg, L. Samuelson, Vertical high-mobility wrap-gated InAs nanowire transistor. *IEEE Electron Device Lett.* **27**, 323 (2006). doi:10.1109/LED.2006.873371
12. J. Zhou *et al*., Piezoelectric-potential-controlled polarity-reversible Schottky diodes and switches of ZnO wires. *Nano Lett.* **8**, 3973 (2008). doi:10.1021/nl802497e Medline
13. W. Z. Wu, Y. G. Wei, Z. L. Wang, Strain-gated piezotronic logic nanodevices. *Adv. Mater.* **22**, 4711 (2010). doi:10.1002/adma.201001925 Medline
14. Z. L. Wang, Nanopiezotronics. *Adv. Mater.* **19**, 889 (2007). doi:10.1002/adma.200602918
15. Z. L. Wang, *Piezotronics and Piezo-Phototronics* (Springer, 2013).
16. Z. L. Wang, Piezopotential gated nanowire devices: Piezotronics and piezo-phototronics. *Nano Today* **5**, 540 (2010). doi:10.1016/j.nantod.2010.10.008
17. Y. Zhang, Y. Liu, Z. L. Wang, Fundamental theory of piezotronics. *Adv. Mater.* **23**, 3004 (2011). doi:10.1002/adma.201100906 Medline
18. Z. L. Wang, Progress in piezotronics and piezo-phototronics. *Adv. Mater.* **24**, 4632 (2012). doi:10.1002/adma.201104365 Medline
19. W. Z. Wu, Z. L. Wang, Piezotronic nanowire-based resistive switches as programmable electromechanical memories. *Nano Lett.* **11**, 2779 (2011). doi:10.1021/nl201074a Medline
20. J. Shi, M. B. Starr, X. D. Wang, Band structure engineering at heterojunction interfaces via the piezotronic effect. *Adv. Mater.* **24**, 4683 (2012). doi:10.1002/adma.201104386 Medline
21. R. S. Johansson, A. B. Vallbo, Tactile sensibility in the human hand: Relative and absolute densities of four types of mechanoreceptive units in glabrous skin. *J. Physiol.* **286**, 283 (1979). Medline
22. Y. G. Wei *et al*., Wafer-scale high-throughput ordered growth of vertically aligned ZnO nanowire arrays. *Nano Lett.* **10**, 3414 (2010).

doi:10.1021/nl1014298 Medline
23. B. Nemeth *et al*., Real-time ion-flux imaging in the growth of micrometer-scale structures and membranes. *Adv. Mater.* **24**, 1238 (2012). doi:10.1002/adma.201104345 Medline
24. S. A. Mascaro, H. H. Asada, Photoplethysmograph fingernail sensors for measuring finger forces without haptic obstruction. *IEEE Trans. Robot. Autom.* **17**, 698 (2001). doi:10.1109/70.964669
25. Z. L. Wang, W. Z. Wu, Nanotechnology-enabled energy harvesting for self-powered micro-/nanosystems. *Angew. Chem. Int. Ed.* **51**, 11700 (2012). doi:10.1002/anie.201201656 Medline

**Acknowledgments:** We thank Y. Zhang for helpful discussions and P. Shao for guidance in using the optical noncontact profilometer. Research was supported by DARPA, Airforce, U.S. Department of Energy, Office of Basic Energy Sciences under Award DE-FG02-07ER46394, NSF, and the Knowledge Innovation Program of the Chinese Academy of Sciences (Grant No. KJCX2-YW-M13).

**Supplementary Materials**
www.sciencemag.org/cgi/content/full/science.1234855/DC1
Materials and Methods
Figs. S1 to S16

7 January 2013; accepted 5 April 2013

Published online 25 April 2013
10.1126/science.1234855

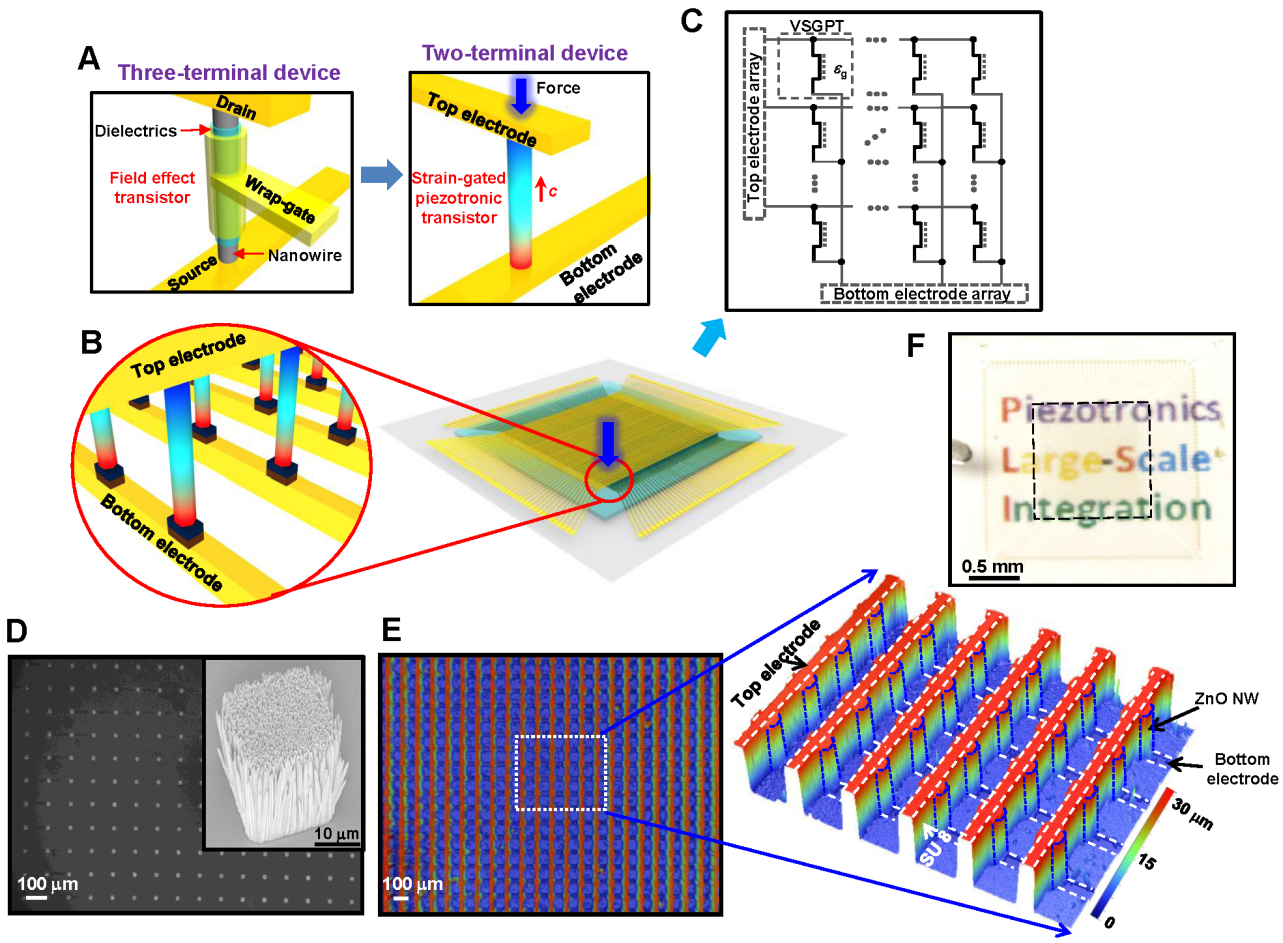


**Fig. 1. Schematic illustration, optical and SEM images, and topological profile image of 3D SGVPT array assembly.** (**A**) Comparison between three-terminal voltage-gated NW FET (left) and two-terminal strain-gated vertical piezotronic transistor (right). Color gradient in strained SGVPT represents the strain-induced piezopotential field, in which red and blue indicate the positive and negative piezopotential, respectively. ZnO NWs in SGVPT grow along the *c* axis, as indicated by the red arrowhead. (**B**) Schematic illustration of a 3D SGVPT array with taxel density of 92 × 92 and scheme for spatial profile imaging of local stress (indicated by the downwards blue arrowhead) by the array (zoom-in schematic). (**C**) Equivalent circuit diagram of the 3D SGVPT array. The region highlighted by black dashed lines is the unit SGVPT device, in which $\varepsilon_g$ represents the mechanical strain gate signal and the vertical dotted line between the two terminals of SGVPT presents the modulation effect of $\varepsilon_g$ on the conducting characteristics of the device. (**D**) SEM image of SGVPT array taken after etching-back the SU 8 layer and exposing top portions (~ 20 μm) of the ZnO NWs. Inset, 30°-tilt view of the exposed ZnO NWs for single taxel. (**E**) Topological profile image of the SGVPT array (Top view). Inset, 3D perspective view of the topological profile image reveals the vertical hierarchy of the SGVPT assembly in which the color gradient represents different heights. (**F**) Optical image of the transparent 3D SGVPT array on flexible substrate. The peripherals are the pads of the device and the central region highlighted by black dashed lines is the active array of 3D SGVPTs.

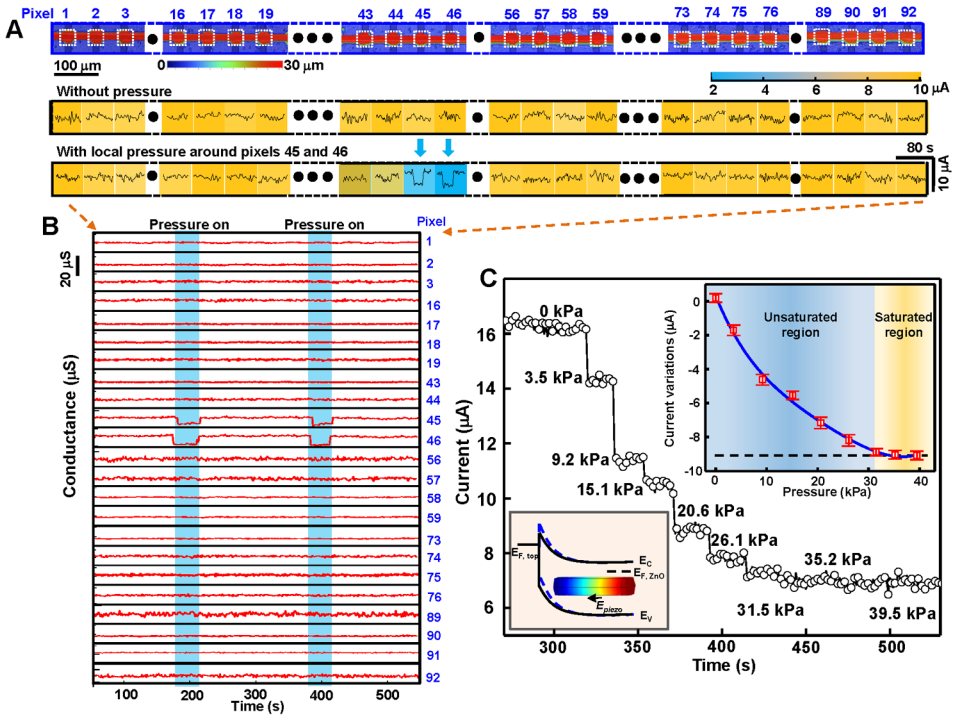


**Fig. 2. Single-channel line-scan (1 × 92) electrical measurement for SGVPT array device.** (**A**) Topological profile images (top view) of 23 selected taxels in a 1 × 92 SGVPT array (single channel) (top frame) and their corresponding current responses (middle and bottom frames) under 1 V bias with and without external stress (20 kPa) applied to certain localized region (around taxels 45 and 46). (**B**) Single-channel conductance measurement in temporal domain illustrating the dynamic response of the 23 selected SGVPT devices in this channel, with and without pressure applied. (**C**) Current responses for taxel 46 under different pressures, presenting the gate modulation effect of applied pressure on the electrical characteristics of SGVPT. Top right inset, current variations (red squares) are plotted versus the applied pressures, clearly showing the saturation of current change when applied pressure is above ~ 30 kPa. Bottom left inset, schematic band-diagram illustrating the change in Schottky barrier height of the reversed biased top contact due to the modulation effect of strain-induced piezopotential. Color gradient represents the distribution of piezopotential field, in which red indicates the positive piezopotential and blue indicates the negative piezopotential. The original band-edges at the reversed biased Schottky contact for the SGVPT device without stress applied are shown in the black solid lines. The band-edges bending at the reversed biased Schottky contact for the SGVPT device with stress applied are shown in the blue dashed lines.

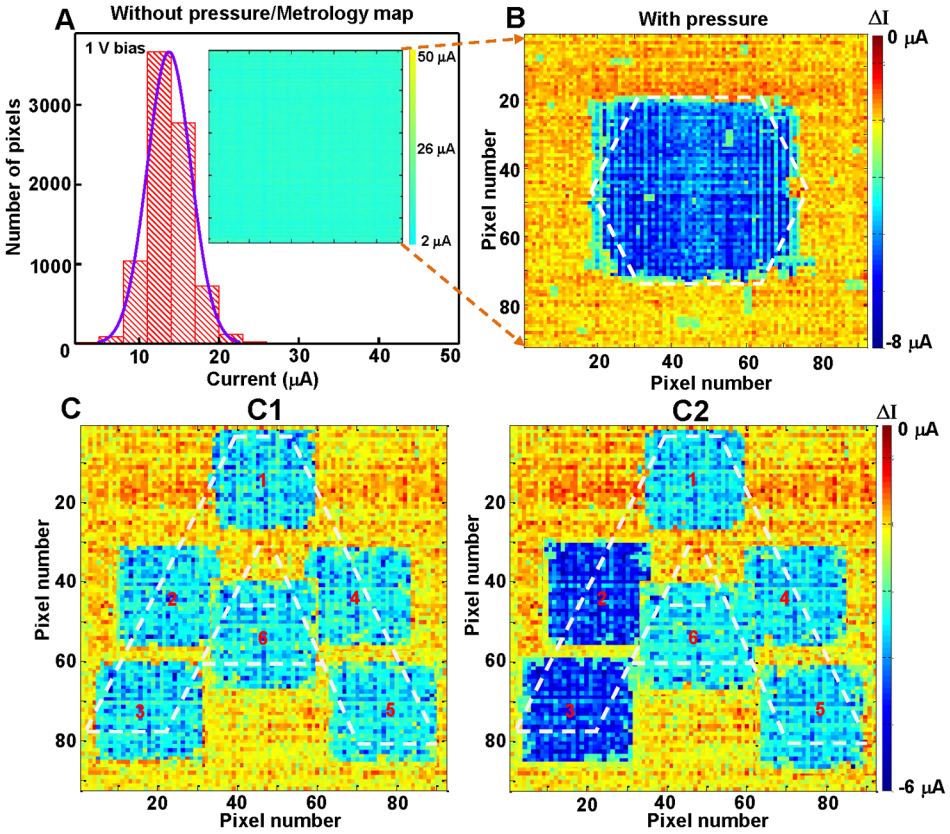


**Fig. 3. Tactile imaging and multi-dimensional sensing by the fully-integrated 92 × 92 SGVPT array.** (**A**) Metrology mapping (Inset) and statistic investigation of the fully integrated SGVPT array without applying stress. (**B**) Current responses contour plot illustrating the capability of SGVPT array for imaging the spatial profile of applied stress. Color bar represents the current differences for each taxel before and after applying the normal stress. The physical shape of the applied stress is highlighted by the white dashed lines. (**C**) Multi-dimensional sensing by SGVPT array exhibits the potential of realizing applications like personal signature recognition with maximum security and unique identity. The calligraphy of written letter “A” is highlighted by the white dashed lines.

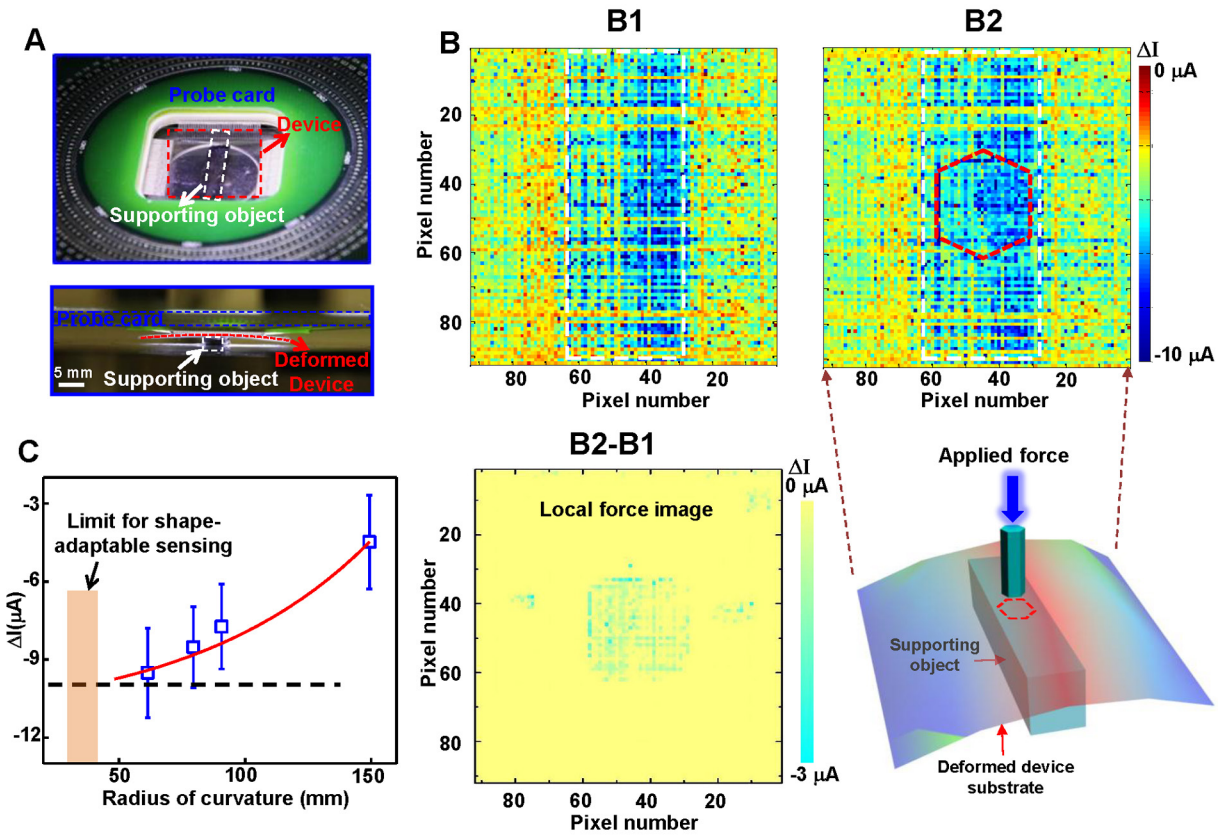


**Fig. 4. Shape-adaptive sensing by the flexible 92 × 92 SGVPT array.** (**A**) Optical photographs of the experimental setup for investigating the feasibility of SGVPT array for shape-adaptive sensing. The top one is the top view of the setup. The bottom one is the side-view of the setup, with the device deformed. (**B**) Shape-adaptive sensing of the SGVPT array. (B1) The measured difference in taxel currents for SGVPT array with and without underneath supporting object. The detected shape change of SGVPT array is illustrated by the dark blue regions and the physical shape of the supporting object beneath the SGVPT device is outlined by the white dashed lines. (B2) The measured variations in taxel current values between bent SGVPT array with extra stress and unstrained SGVPT array. The location/shape of the extra stress is outlined by the red dashed lines. (B2-B1) A clearer demonstration of the data is obtained by numerically subtracting (B1) from (B2), giving rise to spatial imaging of the additionally applied stress when the shape of the SGVPT device is changed. The 3D schematic drawing at the bottom right illustrates the process for shape-adaptive sensing. (**C**) Experimental results showing the limit for shape-adaptable sensing by SGVPT array with current design.